Theses and Dissertations

2017

Computational Study of Jet Flows Emanating from a Circular Orifice

Guanyang Xue
Lehigh University

Follow this and additional works at: http://preserve.lehigh.edu/etd

 Part of the Mechanical Engineering Commons

Computational Study of Jet Flows Emanating

from a Circular Orifice

by

Guanyang Xue

A Thesis

Presented to the Graduate and Research Committee

of Lehigh University

in Candidacy for the Degree of

Master of Science

in

Mechanical Engineering and Mechanics

Lehigh University

May 2017

ii

This thesis is accepted and approved in partial fulfillment of the requirements for the Master of Science.

_____
Date

_____
Thesis Advisor

_____
Chairperson of Department

Acknowledgements

I would like to thank everyone who helped me in this research. First, I want to express my gratitude to my advisor, Prof. Alparslan Oztekin, for all his efforts, especially for him being patience when I faced difficulties in the first few months. Second, I would like to thank Yang Chen. He's been conducting research in the similar field by using Lattice Boltzmann methods. He shared me with his experience about simulations, which accelerated my progress. I'm also grateful to I-Han Liu and Haolin Ma, for their endless support in my graduate life. Furthermore, I want to thank my family, for their continuous encouragement and support during my research.

Contents

List of Tables

List of Figures

Abstract

Computational fluid dynamics simulations are conducted to study jet flows emanating from a circular cross-sectioned orifice. Fluid is injected on a jet into a cuboid domain containing the same fluid at a quiescent state initially. Simulations are performed for a range of Reynolds number from 1050 to 2700 at various instant illustrating the secondary flows induced by well know Kelvin Helmholtz instabilities. Large eddy simulations utilizing Smagorinsky-Lilly turbulence model are performed to characterize the spatial and temporal nature of flow field. *snappyHexMesh* utility is used to discretize the computational domain and *pimpleFoam* solver is used to solve the equations governing the fluid motions. The evolution of velocity and vorticity field is presented on flow images for various values of Reynolds number. It is demonstrated that the nature of secondary flows is strongly dependent on Reynolds number. It is also demonstrated that the evolution and spatial characteristics of secondary flows is strongly dependent on the level of disturbance introduced at the inlet. Our predicted results for the flow field degree agree well with results of experimental observations documented in the literatures validating the mathematical model and the numerical method employed. This study aids in designing and optimizing combustion chambers or designing nozzles including jets emanating from orifices.

Chapter 1

Introduction

1.1 Background

Jet flows are streams of one fluid mixes with a surrounding fluid at rest or in motion. Flows considered in this study are jets emanating from orifice into a large reservoir containing the same fluid at rest. These flows are encountered in many important industrial applications such as fuel injections, heat exchangers and air propulsions. In some of these applications, it is desirable to achieve good mixing. Creation of turbulent structures consisting of large and small eddies will help in achieving good mixing of fluids. The large scale eddies can pull the fluid from surrounding and entrain it to the jet and small scale eddies will help mixing by enhancing diffusion. On the other hand, in some applications it is desirable to avoid creation of turbulent structure since large and small eddies induced by flow transitions can be very unpredictable. They can lead to chaotic and unsustainable behavior of the overall system.

There are numerous experimental studies to investigate characteristics of jet flows. Reynolds(1883), one of the pioneers in fluid dynamics, demonstrated a critical phenomenon transition flow from laminar to turbulent. Later von Karman(1911) discovered the famous Karman vortex street as a manifestation of secondary flows induced by a flow transition. Similar secondary flows are observed as flow structures in free jet flows. More specific ex-

periments on low Reynolds number free jet were performed in the latter half of the 20th century. Becker(1968)[1] found the empirical frequency law of vortex to determine the relation between Reynolds number and the frequency of periodic secondary flows induced by flow transitions. Crow and Champagne(1971)[7] tried to catch the orderly structure of jet flows and discovered several patterns of vortex paring at different Reynolds number. In recent years, with the development of better visualization equipment, researchers examined jet flows emanating more complex shaped orifices. Zaman(2003)[17] worked on lobed nozzle which mixes fluids much faster than a circular one. His results showed that increasing the number of lobes can reduce the turbulence intensity as well as noise, which opened the new era of controllable jets.

Apart from experimental studied of jet flows, the development of more efficient turbulence modeling helps scientists to conduct numerical analyses to study jet flows at higher flow rates and in more complex geometries. Research on turbulence theory started by J. V. Boussinesq(1877)[2]. He proposed the concept of the turbulent viscosity to model the momentum transfer caused by the turbulence, and initiated the quantitative modeling in the area of turbulent flows. L. Prandtl(1904) introduced the concept of a boundary layer and created the wall-bounded model for the turbulent viscosity. A. Kolmogorov(1941)[11] introduced the microscales and established the fundamental of numerical simulations on discretized computational domain. J. Smagorinsky(1963)[19] was the first who created a mathematical model for the turbulent viscosity. Smagorinsky SGS model made large scale numerical simulations to be possible. To overcome the limitation of the original model, few dynamic SGS models were proposed by Germano(1991)[9] and Lilly(1991)[14] separately. An increasing number of models are being constructed since then in pursuit of better accuracy and stability of computational fluid dynamic simulations of turbulent flows.

There still are several outstanding issues and challenges about these flows that are needed to be addressed. Formation of large and small scale eddies induced by flow transitions are strongly dependent on the shape of orifice and the nature of disturbances in the system. Our objective is to attain high level of mixing at relatively small flow rates. Several studies

have been conducted to examine evolution of vortices as jet introduced form orifices. The formation of vortices is manifestation of well-known flow transition in these systems. The vortices are formed slightly after the orifice as the intensity of vortices increases they roll up and eventually break down. Todde, Spazzini and Sandberg(2009)[20] did a series of physical experiments focusing on low Reynolds number free jets emanating from circular orifices and documented results that characterize the flow field very well. We conducted simulations in a computational domain that mimics the experimental setup. We compare our results against their experimental results. That helps to validate the mathematical model and numerical methods employed here. The method can then be extended to study jet flows emanating from orifices of different shape and size at low values of Reynolds number. Fundamental understanding of these flows will help engineers to design and optimize systems involving jet flows.

Chapter 2

Mathematical Model

Large Eddy Simulation (LES) was initially proposed by Joseph Smagorinsky(1963)[19] and explorered by Deardorff(1970)[8]. LES turbulence model is widely used as a CFD tool to study complex transient turbulent flows in three-dimensional geometries. Turbulent flows can be simulated by Direct Numerical Simulation (DNS), which is the most accurate method theoretically. However nowadays DNS still requires memory well beyond the capabilities of workstations or clusters. They cannot accommodate meshes at Kolmogorov length scale[11] in their limited memory.

LES, on the other hand, separates the velocity field into resolved and sub-grid part. In resolved part the large eddies are calculated as usual, while small eddies are treated separately with sub-grid scale models. By filtering structures with small length scales, the cost of simulations is reduced significantly.

2.1   LES Filter

LES filter is a low-pass filter, which is defined by a convolution on a spatial field.[22]

$$\bar{\phi}(\boldsymbol{x}) = \iiint G(\boldsymbol{x} - \boldsymbol{\xi}; \Delta)\phi(\boldsymbol{\xi}, t)\, \mathrm{d}^3\boldsymbol{\xi} \tag{2.1}$$

G is the convolution kernel based on distinct types of filters. Leonard (1975)[12] defined a box filter

$$G(\boldsymbol{x} - \boldsymbol{\xi}; \Delta) = \begin{cases} \dfrac{1}{\Delta^3}, & |\boldsymbol{x} - \boldsymbol{\xi}| < \dfrac{\Delta}{2} \\ 0, & \text{otherwise} \end{cases} \tag{2.2}$$

OpenFOAM uses a modified box filter[6] by default. The kernel is defined naturally from a finite volume method by

$$G(\boldsymbol{x} - \boldsymbol{\xi}) = \begin{cases} \dfrac{1}{V}, & \boldsymbol{\xi} \in V \\ 0, & \text{otherwise} \end{cases} \tag{2.3}$$

where V is the cell from finite volume discretization. This gives

$$\bar{\phi}(\boldsymbol{x}) = \frac{1}{|V|} \int_V \phi(\boldsymbol{\xi}) \mathrm{d}\boldsymbol{\xi} \tag{2.4}$$

The above formula shows that LES filtering in OpenFOAM can't handle 2D problems, since 2D cases does not have a real volume. We have tried several simulations for two-dimensional geometries and did not attain a proper filtering of small scale structures.

2.2 Filtered Incompressible Equations

The momentum equation using the Einstein notation is

$$\frac{\partial u_i}{\partial t} + \frac{\partial u_i u_j}{\partial x_j} + \frac{1}{\rho} \frac{\partial p}{\partial x_i} - \nu \frac{\partial^2 u_i}{\partial x_j \partial x_j} \tag{2.5}$$

Filtering the Equation 2.5 results in

$$\overline{\frac{\partial u_i}{\partial t}} + \overline{\frac{\partial u_i u_j}{\partial x_j}} + \frac{1}{\rho} \overline{\frac{\partial p}{\partial x_i}} - \nu \overline{\frac{\partial^2 u_i}{\partial x_j \partial x_j}} = 0$$

From the properties of convolution

$$\frac{\partial \bar{u}_i}{\partial t} + \frac{\partial \overline{u_i u_j}}{\partial x_j} + \frac{1}{\rho} \frac{\partial \bar{p}}{\partial x_i} - \nu \frac{\partial^2 \bar{u}_i}{\partial x_j \partial x_j} = 0$$

The nonlinear convection term $\dfrac{\partial \overline{u_i u_j}}{\partial x_j}$ is difficult to evaluate directly. Introducing $\tau_{ij} = \overline{u_i u_j} - \bar{u}_i \bar{u}_j$, we obtain the standard LES equations:

$$\frac{\partial \bar{u}_i}{\partial t} + \bar{u}_j \frac{\partial \bar{u}_i}{\partial x_j} + \frac{1}{\rho}\frac{\partial \bar{p}}{\partial x_i} - \nu \frac{\partial^2 \bar{u}_i}{\partial x_j \partial x_j} + \frac{\partial \tau_{ij}}{\partial x_j} = 0 \tag{2.6}$$

2.3   Sub Grid Scales Models

By employing the Boussinesq approximation[2], the SGS stress can be calculated by

$$\tau_{ij} = -2\nu_t \bar{S}_{ij} + \frac{1}{3}\tau_{kk}\delta_{ij} \tag{2.7}$$

where $\bar{S}_{ij} = \dfrac{1}{2}\left(\dfrac{\partial \bar{u}_i}{\partial x_j} + \dfrac{\partial \bar{u}_j}{\partial x_i}\right)$ is the rate-of-strain tensor and ν_t is the turbulent viscosity.

Substitute the stress into momentum equation we have

$$\frac{\partial \bar{u}_i}{\partial t} + \bar{u}_j \frac{\partial \bar{u}_i}{\partial x_j} + \frac{1}{\rho}\frac{\partial \bar{p}}{\partial x_i} - \frac{\partial}{\partial x_j}\left[(\nu + \nu_t)\frac{\partial \bar{u}_i}{\partial x_j}\right] = 0 \tag{2.8}$$

In Smagorinsky model,

$$\nu_t = (C_s \Delta)^2 |\bar{S}| \tag{2.9}$$

where

Δ is the filter size, OpenFOAM uses $\Delta = \sqrt[3]{V}$.

C_s is a constant usually between 0.1 and 0.2. OpenFOAM takes $C_s = 0.167$ by default.

$\bar{S} = \sqrt{2\bar{S}_{ij}\bar{S}_{ij}}$. Here the definition of $\bar{S}$ is different from textbook[19] , due to a distinct programming implementation in OpenFOAM.

2.4   *pimpleFoam* Solver

A transient solver must be chosen for LES simulations. For incompressible turbulent flows, we may use either *pisoFoam* or *pimpleFoam*. Since the simulation focus on time averaged statistics, a slightly larger Courant number can still provide enough accuracy.

Therefore we choose *pimpleFoam* solver for better numerical stability.

2.4.1   Momentum Predictor

For incompressible flow, there's no pressure equation therefore we need to derive it from continuity equation.

From the momentum equation

$$\frac{\partial \boldsymbol{U}}{\partial t} + \nabla \cdot (\boldsymbol{U} \otimes \boldsymbol{U}) = -\nabla p + \nabla \cdot (\nu \nabla \boldsymbol{U}) \tag{2.10}$$

Here p is scaled to ρ.

The momentum equation is discretized as[13]

$$\int \int \frac{\partial \boldsymbol{U}}{\partial t} dV dt = (\boldsymbol{U}_p^r - \boldsymbol{U}_p^n) V_p \tag{2.11}$$

$$\int \int \nabla \cdot (\boldsymbol{U} \otimes \boldsymbol{U}) dV dt = \int \int \boldsymbol{U} \otimes \boldsymbol{U} dS dt = \sum (\Phi^n \boldsymbol{U}_f^r) \Delta t \tag{2.12}$$

$$\int \int \nabla \cdot (\nu \nabla \boldsymbol{U}) dV dt = \int \int \nu \nabla \boldsymbol{U} dS dt$$
$$= \sum \nu (\nabla \boldsymbol{U}^r)_f \boldsymbol{S}_f \Delta t = \sum \left(\nu |\boldsymbol{S}_f| \frac{\boldsymbol{U}_N^n - \boldsymbol{U}_P^n}{|d|} \right) \Delta t \tag{2.13}$$

where superscript ^{n} is the current time step and superscript ^{r} denotes the predicted time step. Subscript $_f$ represents the value on cell surface, subscripts $_P$ and $_N$ represent the present and the neighboring cells, respectively.

Substitute the discretization properties into the momentum equation gives

$$\frac{\boldsymbol{U}_p^r - \boldsymbol{U}_p^n}{\Delta t} V_p + \sum (\Phi^n \boldsymbol{U}_f^r) = \sum \nu |\boldsymbol{S}_f| \frac{\boldsymbol{U}_N^n - \boldsymbol{U}_P^n}{|d|} - \nabla p^n \tag{2.14}$$

Suppose we are using central differencing scheme to interpolate the velocity on a cell surface

$$\boldsymbol{U}_f^r = \frac{\boldsymbol{U}_P^r - \boldsymbol{U}_N^r}{2} \tag{2.15}$$

8

we have

$$A_P \boldsymbol{U}_P^r + \sum A_n \boldsymbol{U}_N^r - E_P^n = -\nabla p^n \tag{2.16}$$

where

$$
\begin{aligned}
A_P &= \frac{V_p}{\Delta t} + \sum \frac{\Phi_f^n}{2} + \sum \left(\nu \frac{|\boldsymbol{S}_f|}{|d|} \right) \\
A_N &= \frac{F_f^n}{2} - \nu \frac{|\boldsymbol{S}_f|}{|d|} \\
E_P &= \frac{V_P}{\Delta t} \boldsymbol{U}_P^n
\end{aligned}
\tag{2.17}
$$

To solve the predicted velocity $\boldsymbol{U}_P^r$, neglect the pressure gradient term

$$\boldsymbol{U}_P^r = \frac{1}{A_P} \left(-\sum A_n \boldsymbol{U}_N^r + E_P^n \right) \tag{2.18}$$

However the velocity field $\boldsymbol{U}^r$ does not satisfy the continuity equation. We need to derive a corrected velocity field $\boldsymbol{U}^{n+1}$.

To satisfy the continuity equation

$$\nabla \cdot \boldsymbol{U}_P^{n+1} = 0 \tag{2.19}$$

we have the following from the definition of divergence

$$\sum (\boldsymbol{U}_F^{n+1} \cdot \boldsymbol{S}_f) = 0 \tag{2.20}$$

by applying discretization we obtain

$$\sum \left[\left(\boldsymbol{U}_{P,f}^{n+1} - \frac{1}{A_{P,f}} \nabla_f p^{n+1} \right) \cdot \boldsymbol{S}_f \right] = 0 \tag{2.21}$$

moving terms gives

$$\sum \boldsymbol{U}_{P,f}^{n+1} \cdot \boldsymbol{S}_f = \sum \left(\frac{1}{A_{P,f}} \nabla_f p^{n+1} \right) \cdot \boldsymbol{S}_f \tag{2.22}$$

9

i.e.

$$\nabla \cdot \boldsymbol{U}_{P,f}^{n+1} = \nabla \cdot \left(\frac{1}{A_{P,f}} \nabla p^{n+1} \right) \tag{2.23}$$

2.4.2   Merged PISO-SIMPLE algorithm

PIMPLE algorithm, which is created by OpenFOAM, is a combination of SIMPLE and PISO. First it searches a steady solution with under-relaxation as SIMPLE correction, which is called the outer loop. After the tolerance is reached we use PISO correction to calculate the time derivative term as the inner loop.

- *pimpleFoam* main program[15]:

```
for (int oCorr=0; oCorr<nOuterCorr; oCorr++)
{
    #include "UEqn.H"
    for (int corr=0; corr<nCorr; corr++)
    {
        #include "pEqn.H"
    }
}
```

- UEqn.H:

  1. Derive $\boldsymbol{U}$ equation

```
tmp<fvVectorMatrix> UEqn
(
    fvm::ddt(U)
  + fvm::div(phi, U)
  + turbulence->divDevReff(U)
);
```

  2. Skip the relaxation for the last outer correction

```
if (oCorr == nOuterCorr −1)
{
    UEqn().relax(1);
}
else
{
    UEqn().relax();
}
```

3. Calculate coefficient A_P

```
volScalarField rUA = 1.0/UEqn().A();
```

4. Solve U directly or through momentum predictor

```
if (momentumPredictor)
{
    solve(UEqn() == −fvc::grad(p));
}
else
{
    U = rUA*(UEqn().H() − fvc::grad(p));
}
```

- pEqn.H

    1. Calculate U

```
U = rUA*UEqn().H();
```

    2. Calculate flux

```
phi = (fvc::interpolate(U) & mesh.Sf())
    + fvc::ddtPhiCorr(rUA, U, phi);
```

3. Choose relaxation or PISO

```
if (oCorr != nOuterCorr-1)
{
    p.relax();
}
U -= rUA*fvc::grad(p);
```

Chapter 3

Simulation Setup

3.1 Reference Experiment
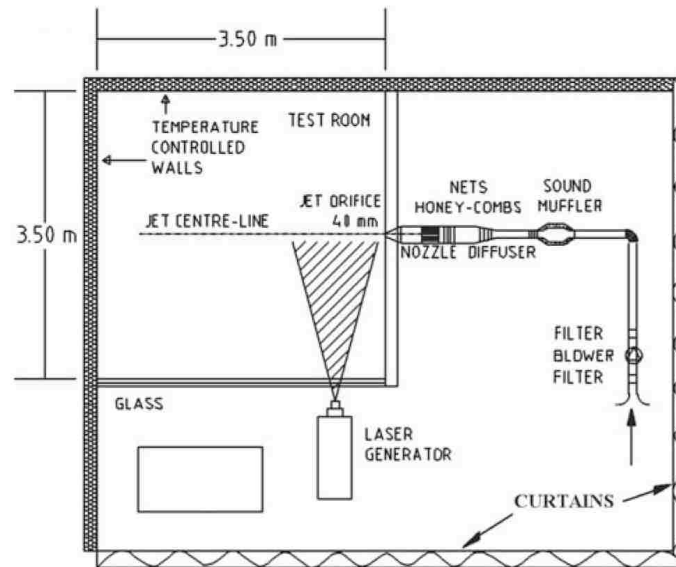
Figure 3.1: Schematic of the reference experimental setup[20].

The reference experiment was performed in a $3.5 \times 3.5 \times 2.5 m^3$ temperature controlled room, as shown in Figure 3.1. The jet emanates from a circular cross-sectioned nozzle of $0.04m$ diameter in to a room. The flow is driven by a centrifugal fan with proper insulation to provide a steady airflow. Air leaves the room without forcing through slits located on

the wall opposite to the inlet, minimizing the effect of boundary conditions on the jet flow near the orifice. The velocity measurement was performed by an anemometric bridge which records data at 2048 Hz. The average velocity at the center, the turbulent intensity, the fluctuating velocity signals and the spectra were analyzed were presented.

3.2   Numerical Simulation

Experimental results illustrate that the key length scale for development and dissipation of turbulent structures is about $0.2m \times 0.2m \times 0.8m$. With proper boundary condition settings we can simulate jet flows observed in the experiment in a much smaller computational domain to reduce the burden on the computational resources. Large eddy simulations employing Smagorinsky model are used to conduct computational fluid dynamics simulations in a three dimensional geometry. The mesh has a refined inner area where $\Delta x \approx 1mm$, and a coarse outer area, where $\Delta x \approx 4mm$. The time step is adaptive, that is determined by a maximum value of the Courant number automatically. In order to ensure the accuracy and the stability, OpenFOAM is compiled in double precision. For further analysis, the centerline velocity data is interpolated and saved every 0.002s (500 Hz sampling).

3.2.1   Hardware

All simulations were executed on a dual Intel Xeon E5-2670@2.60GHz (8 cores, 16 threads) with 128 GB DDR3-1600 ECC Registered Memory. Typically, computational fluid dynamics simulations are memory-limited and thus the memory bandwidth is the bottleneck. Each Intel E5 CPU has 4 memory channels providing 51.2GB/s bandwidth. CPUs are connected by an 8GT/s (32GB/s equivalent) QPI link. Comparing to consumer-level CPU and RAM, these enterprise-level parts shows better stability for long time simulations.

3.2.2   Software

The operating system is Ubuntu 16.04 LTS and all cases were simulated by OpenFOAM 4.1. The STL file were generated by SALOME 7.8.0 and the post-processing results were

processed by MATLAB R2016b and rendered by ParaView 5.0.1. MATLAB runs under academic license while all other software are open source to avoid the cost of license.
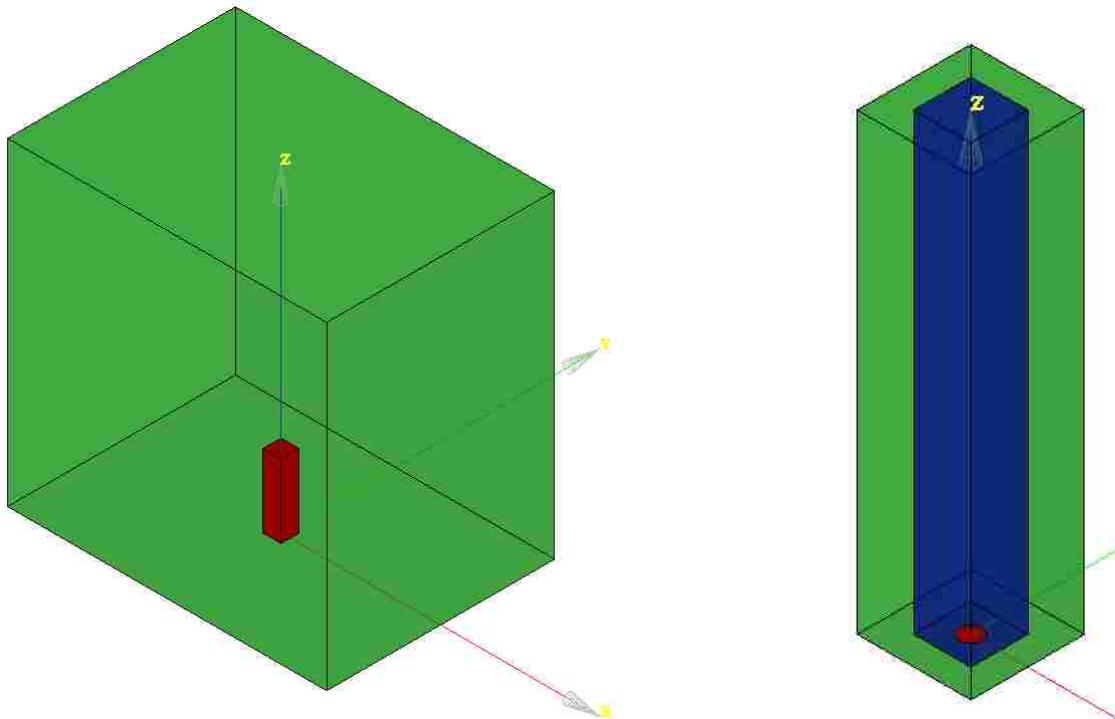
(a) Experiment room(green) v.s. simulation domain(red)

(b) Coarse area(green) and refined area(blue)

Figure 3.2: Schematic of the computational domain.

3.3   Pre-processing

3.3.1   Base Mesh

snappyHexMesh utility requires a coarse base mesh for snapping. To achieve a resolution of $1mm$ for refined mesh, we first generate a $50 \times 50 \times 200$ cuboid base mesh simply by *blockMesh* utility then refine it by 4 times.

3.3.2   STL File

A STereoLithography (STL) file is used to describe the outline of orifice. This format can be generated easily by all major CAE software including open source software SALOME,
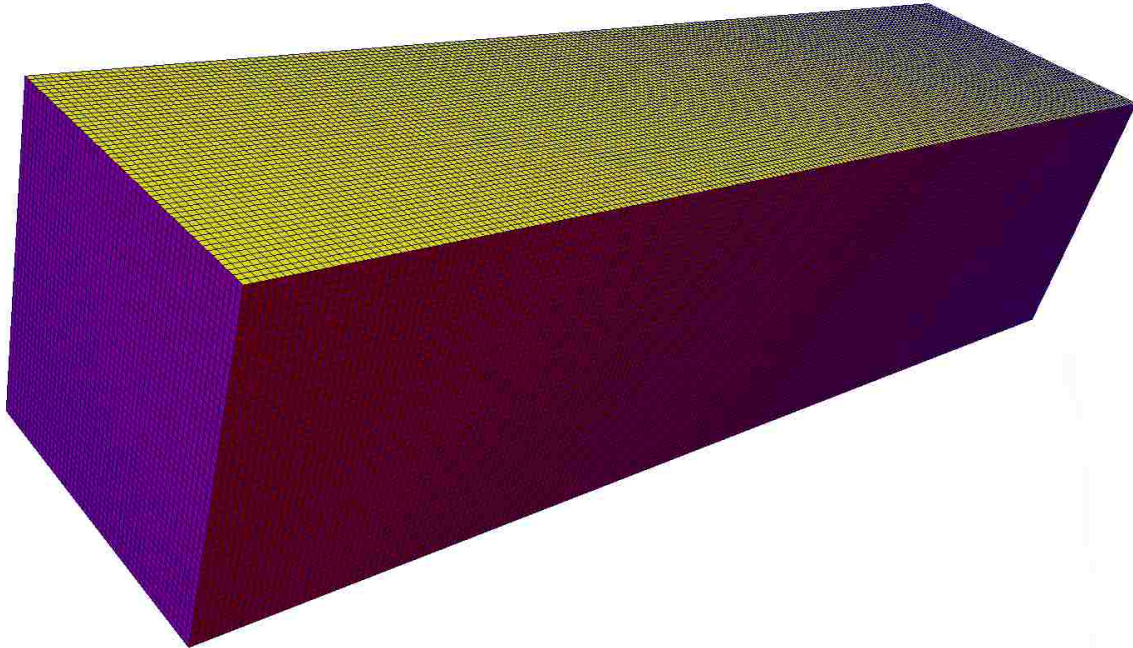
Figure 3.3: Discretized domain with $50 \times 50 \times 200$ coarse base mesh

or we can even produce one by C or MATLAB since it requires an ASCII plain text with a simple grammar. *snappyHexMesh* accepts STL file as a tessellation instruction so that we can generate meshes with any specific orifice shape.

3.3.3   *snappyHexMesh*

To maximize the efficiency of calculation, only the center of the domain should be refined. We pick the box area from $[-0.05, -0.05, 0]$ to $[0.05, 0.05, 0.8]$ to have a 4x refinement, leaving the rest of mesh untouched. This will save nearly 3/4 of the memory and more computation time comparing to a $200 \times 200 \times 800$ full size mesh.

3.3.4   Mesh Decomposition

In order to run the simulation on multi cores, the mesh should be decomposed so that each core processes its own part. The machine has 16 cores/32 threads. However for CPU-bound tasks, a hyper-threading will significantly decrease the performance. Here we divide the box into 16 equivalent subdomains. The simplest way to accomplish that is to bisect
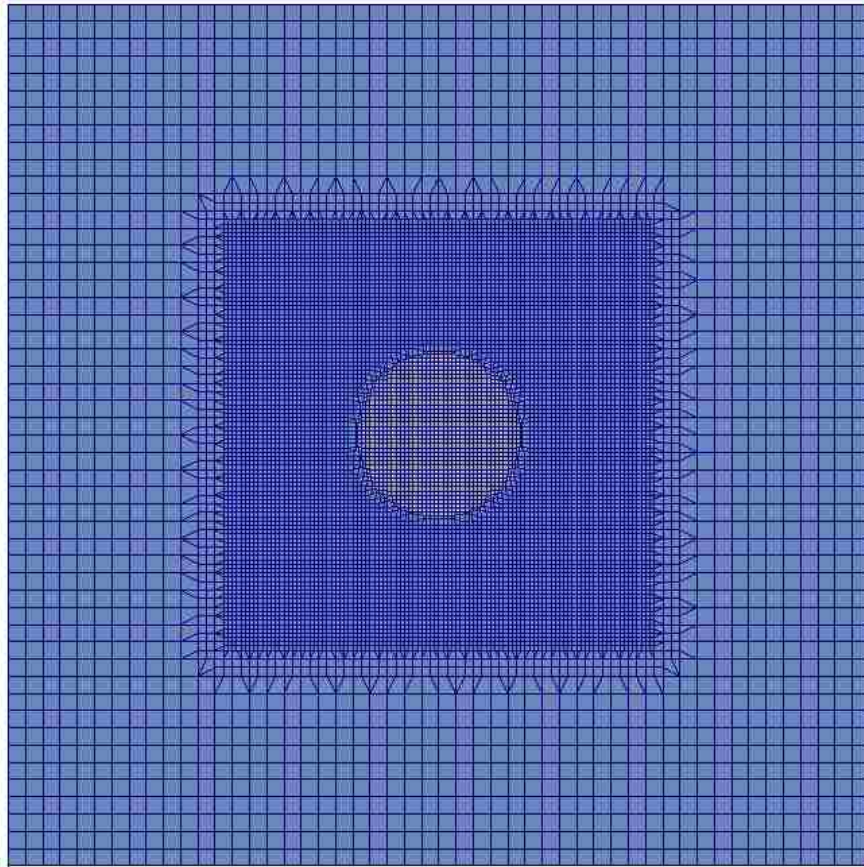
Figure 3.4: Structured mesh shown in cross-sectional view (XoY plane view)
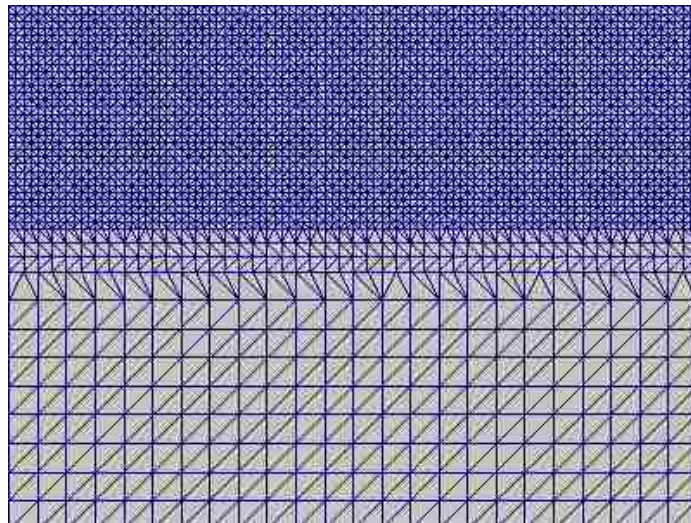
Figure 3.5: Structured mesh shown in YoZ plane view

$x\&y$ axis and quadrisect z axis to have a minimum boundary for each subdomain. The smaller the processor boundaries are, the higher the efficiency the decomposition will be.

3.4 Boundary Conditions

3.4.1 Bottom (without inlet)

U (Velocity)

Considering viscous effect, the velocity on the wall should be 0. There's a built-in *noslip* boundary condition that can be imposed on the velocity field.

$$\boldsymbol{U} = 0 \tag{3.1}$$

p (Pressure)

The normal derivative of pressure on the wall should be zero thus a *zeroGradient* type of boundary condition is applied.

$$\frac{\mathrm{d}p}{\mathrm{d}\boldsymbol{n}} = 0 \tag{3.2}$$

ν_t (Turbulent Viscosity)

We cannot let OpenFOAM calculate the turbulent viscosity ν_t using the Smagorinsky model, that generates discontinuity or even oscillation at the edge of the inlet and leads to a numerical instability. To avoid that, we need to apply a continuous wall function. From the log law of the wall[21]

$$u = \frac{u_\tau}{\kappa} \ln E y^+ \tag{3.3}$$

where

$u_\tau = \sqrt{\dfrac{\tau_\omega}{\rho}}$, τ_ω is the wall shear stress

κ is the Kármán constant, where $\kappa \approx 0.41$[10]

$E = 9.8$

y^+ is the non-dimensional distance.

Jonas(2000)[3] shows that the turbulent eddy viscosity can be obtained by

$$\nu_t = \nu \left(\frac{y^+ \kappa}{\ln Ey^+} - 1 \right) \tag{3.4}$$

OpenFOAM provides *nutUWallFunction* to create a smooth near wall ν_t from the above equation.

3.4.2 Inlet

U

To run a LES simulation under low Reynolds number and obtain a flow transition in a relatively short flow time, disturbances with finite amplitude have to be added at the inlet[5]. Otherwise the jet flow will go straight towards the outlet without formation of the secondary flows induced by flow transitions. One traditional approach is extending the inlet to make the flow fully developed. Another easy method is to add a small amount of random noise at inlet velocity. In OpenFOAM there's a built-in boundary condition *turbulentInlet* defined by

$$\boldsymbol{U}_p^n = (1 - \alpha)\boldsymbol{U}_p^{n-1} + \alpha(\boldsymbol{U}_{ref} + C_{RMS} \cdot s \cdot |\boldsymbol{U}_{ref}|) \tag{3.5}$$

where

$\boldsymbol{U}_p$ is the calculated patch value.

$\boldsymbol{U}_{ref}$ is the reference patch value, in this case determined by Reynolds number.

α is the relaxation factor, default $\alpha = 0.1$.

$C_{RMS} = \sqrt{12(2\alpha - \alpha^2)}/\alpha = 16.1$ is correction factor of root mean square fluctuation.

s is the randomly generated fluctuation, which is a white noise.

With this procedure the random disturbance is evenly distributed not only on its value, but also on RMS and the spectrum.

p

As the Dirichlet type of boundary condition is set for velocity at the inlet, the inlet pressure should be set as a Neumann type of boundary condition. Thus *zeroGradient* condition should be applied at the inlet for the pressure field.

$$\frac{\mathrm{d}p}{\mathrm{d}\boldsymbol{n}} = 0 \tag{3.6}$$

ν_t

For inlet patch the turbulent viscosity is calculated by OpenFOAM automatically via *calculated* B.C. type.

3.4.3 Outlet

U

The intuitive boundary condition on the outlet is *zeroGradient*. However reverse flow may occur. To prevent the occurrence of a reverse flow, a special outlet BC for velocity has to be applied. We have tested *inletOutlet*. It can reduce the magnitude of reverse flow but it still has flaws in extreme conditions. The final boundary condition we chose is *pressureInletOutletVelocity* which is defined as

$$\begin{cases} \dfrac{\mathrm{d}\boldsymbol{U}}{\mathrm{d}\boldsymbol{n}} = 0 & \text{for outflow} \\ \boldsymbol{U}_{tangent} = 0 & \text{for inflow} \end{cases} \tag{3.7}$$

p

Theoretically there's no need to calculate pressure for incompressible flow. However OpenFOAM requires a specific pressure value for calculation. Again if we apply the easiest *fixedValue* reverse flow will occur. Therefore we set the total pressure at the outlet. In

OpenFOAM the *totalPressure* specifies

$$\begin{cases} p = p_0 & \text{for outflow} \\ p = p_0 - \dfrac{1}{2}|\boldsymbol{U}|^2 & \text{for inflow} \end{cases} \tag{3.8}$$

ν_t

Outlet turbulent viscosity is the same as inlet.

3.4.4 Sides

There are three choices of boundary conditions: the wall, the symmetric and the periodic.

The wall B.C. has a strong effect to decelerate the flow. The only way to apply wall B.C. is to make enough clearance between flow area and side patches, which will make the computational domain to be very large.

The symmetric B.C. has no friction problem but it does not make sense. After a long time simulation the flow will be attracted by its own mirror, as Venturi effect elaborates.

The periodic B.C. is an ideal choice for this situation. It is equivalent to infinite equidistant inlets on the bottom surface which makes sense in real world. With periodic boundary condition imposed on the velocity field we obtain the jet flow structures that are very similar to those observed in the experiment.

3.5 Initial Conditions

Usually we use potentialFoam or simpleFoam to build up the velocity and the pressure field. However, steady-state flow solvers are not applicable to LES turbulence model since the flow is inherently transient. They will generate a similar result to RANS, which still lacks of large and small scale eddies. Therefore, in this study we have to set the fluid in the domain at rest initially.

3.6 Post Processing

The mesh has around 9 million nodes and it occupies nearly 1 GB disk space to store information about the velocity and the pressure field at one time step. That makes impossible to save data at all time steps. However we only need to interpolate velocity on YoZ plane slice and save them every 0.05s(20fps) for visualization. These Visualization ToolKit (vtk) files only uses several megabytes for each slice. Furthermore a centerline velocity is also stored every 0.002s(500fps) in plain text files for further analysis.

Chapter 4

Simulation Analysis

4.1   Disturbance Level

As mentioned before in Section 3.4.2, a random noise needs to be added at the inlet
to capture secondary flow structure induced by Kelvin Helmotz instabilities. Magnitude
of disturbances introduced at the inlet strongly influences the growth and the dissipation
of large and small scale turbulence structures at a given Reynolds number. If the level of
disturbances is too small, either very lengthy channel is required or very long simulation time
is needed. Either situation is not practical since it requires unrealistic level of computational
resources to perform simulations. The magnitude of disturbances is adjusted based on the
selected Reynolds number of the jet flow. We determine the relationship between Reynolds
number and disturbance level.

We applied bisection method to select the proper random noise strength so that the
decay tendency of centerline mean velocity profile can match the reference experiment.
Computational fluid dynamics simulations are conducted for various values of Reynolds
number as listed in Table 4.1. For each value of Re, the magnitude of disturbance applied
at the inlet is listed.

Applying regression analysis, the relationship with the magnitude of disturbance and

Inlet velocity	Reynolds number	Noise amount	Disturbance level
0.4m/s	1050	0.04	10.0%
0.5m/s	1350	0.032	6.40%
0.6m/s	1620	0.028	4.67%
0.8m/s	2175	0.014	1.75%
1.0m/s	2750	0.007	0.70%

Table 4.1: Random noise ratio as a function of the inlet velocity or Reynolds number.

Reynolds number is determined for the range of Reynolds number selected:

$$f(x) = 46.51 \cdot e^{-0.001461x}$$

The above formula only applies to a specific fluid. With this empirical relation we can simulate jet flows emanating from orifice of different shape and size.
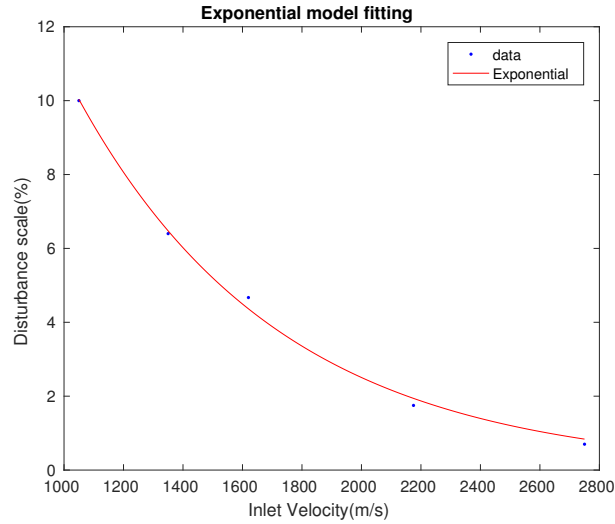
Figure 4.1: Regression analyses for random noise as a function of the inlet velocity.

4.2   Flow Visualization

In order to characterize the flow structure its topology, both instantaneous and time-averaged velocity and vorticity fields are presented.

The jet emanates from the circular nozzle at a uniform velocity $\boldsymbol{U}_0$. The fluid speed
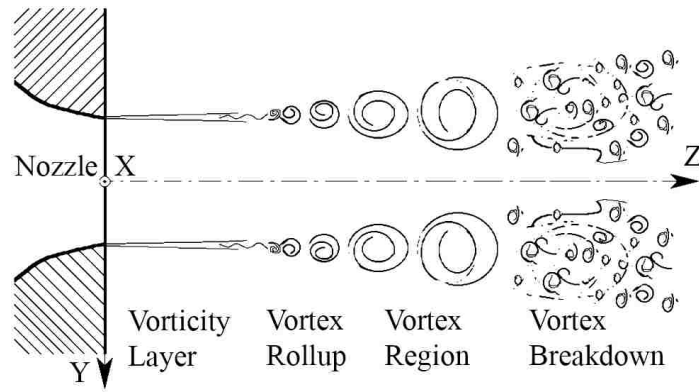
Figure 4.2: Schematic of free jet flows[20].

(a) Time-averaged velocity

(b) The standard deviation of velocity

(c) Time-averaged vorticity

Figure 4.3: Contours of temporal statistic sperformed for Re=1620. Images are acquired at YoZ plane for $x = 0$.
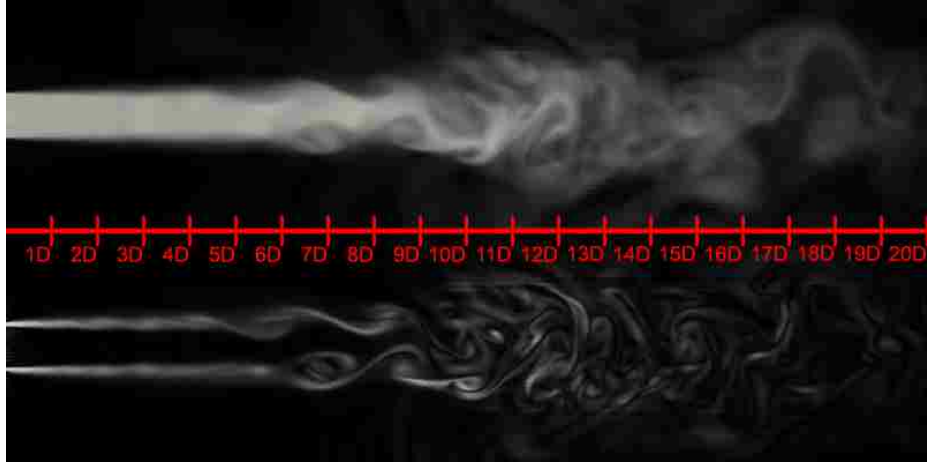
(a) Re=1050
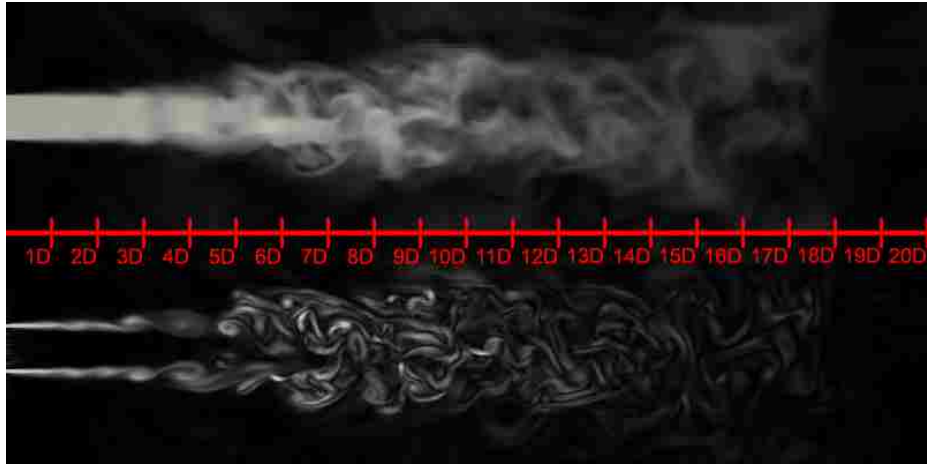
(b) Re=1620
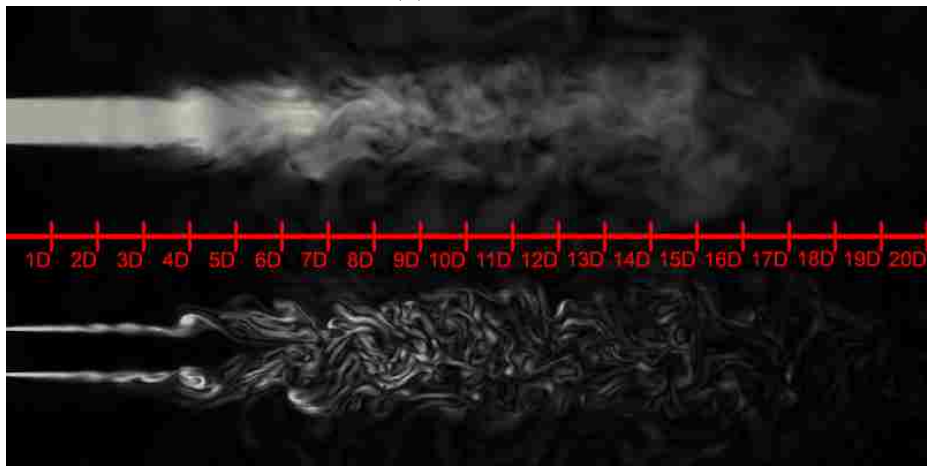
(c) Re=2700

Figure 4.4: A pair of contours of instantaneous velocity (the top image) and instantaneous vorticity (the bottom image). Images are acquired at YoZ plane for $x = 0$.

in the core region of the jet has the highest average and the lowest standard deviation, indicating that the fluid moves steadily in the stream-wise direction in the jet core. The fluid in the outer region of the jet slows down by the fluid at the surrounding; forming a free shear layer as Figure 4.3c. The rolling vortices are formed at the outer region of the jet. The rolling vortex is thinner near the orifice while the width of the vorticity layer grows but the strength weakens away from the orifice. This illustrates the onset of the roll up stage of small vortices. The size of the vortices grows almost linearly in the stream-wise direction before vortex breakdown and the width of the core jet increases linearly as well, which forms a cone zone. Instantaneous images of the flow field shows that that vortices propagates downstream along with the core jet. A comparable image documented by O'Neill(2004)[18] has a similar near-orifice zone in jet flows at Reynolds number of 1030.

4.2.1 Cross-sectional view

Contours of velocity and vorticity fields are acquired at various cross-sections in the stream-wise direction. These images help to understand evolution of secondary flows induced by flow transitions and they provide a new perspective to examine the flow structure near the orifice.

In the region within $X/D = 4$ both velocity and vorticity are coaxial. In this region a solid circle of high flow region is observed and the vorticity layer manifests itself as a sharp ring. There is a clear indication of diffusion in the region near the outer edge of the core. From $X/D = 5$, where velocity decays in for Re=1620, the fluid enters the vortex region. The flow pattern are no longer coaxial, showing that large vortices are detaching in this region. After $X/D = 8$ it is illustrated that vortices appear in the cross-sectional plane, which indicates that the vortex break down occurs and vortices break down into smaller disordered vortices.

(a) 1D   (b) 2D   (c) 3D

(d) 4D   (e) 5D   (f) 6D

(g) 7D   (h) 8D   (i) 9D
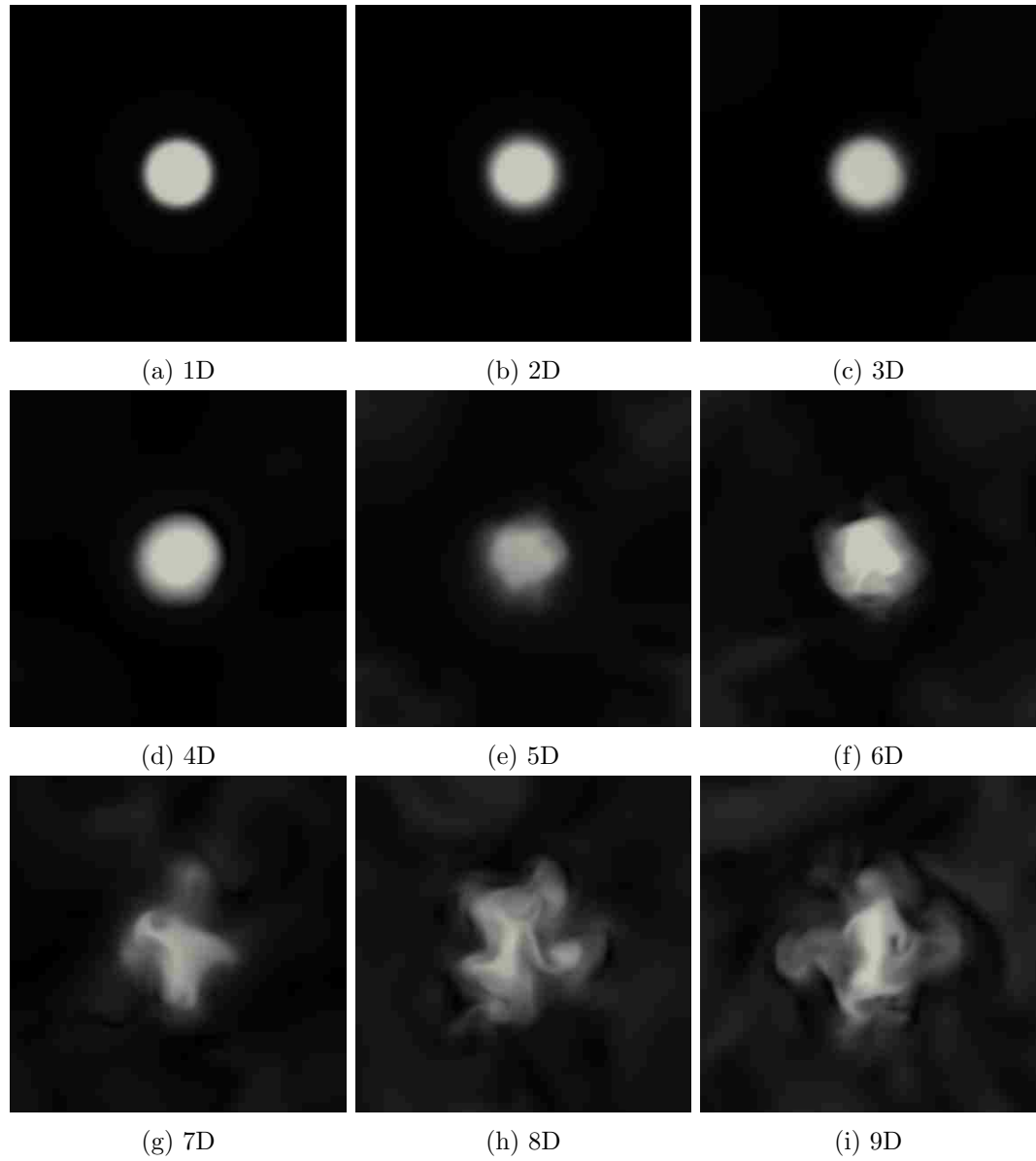
Figure 4.5: Contours of instantaneous velocity for Re = 1620. Images are acquired at appointed cross-sections away from orifice.
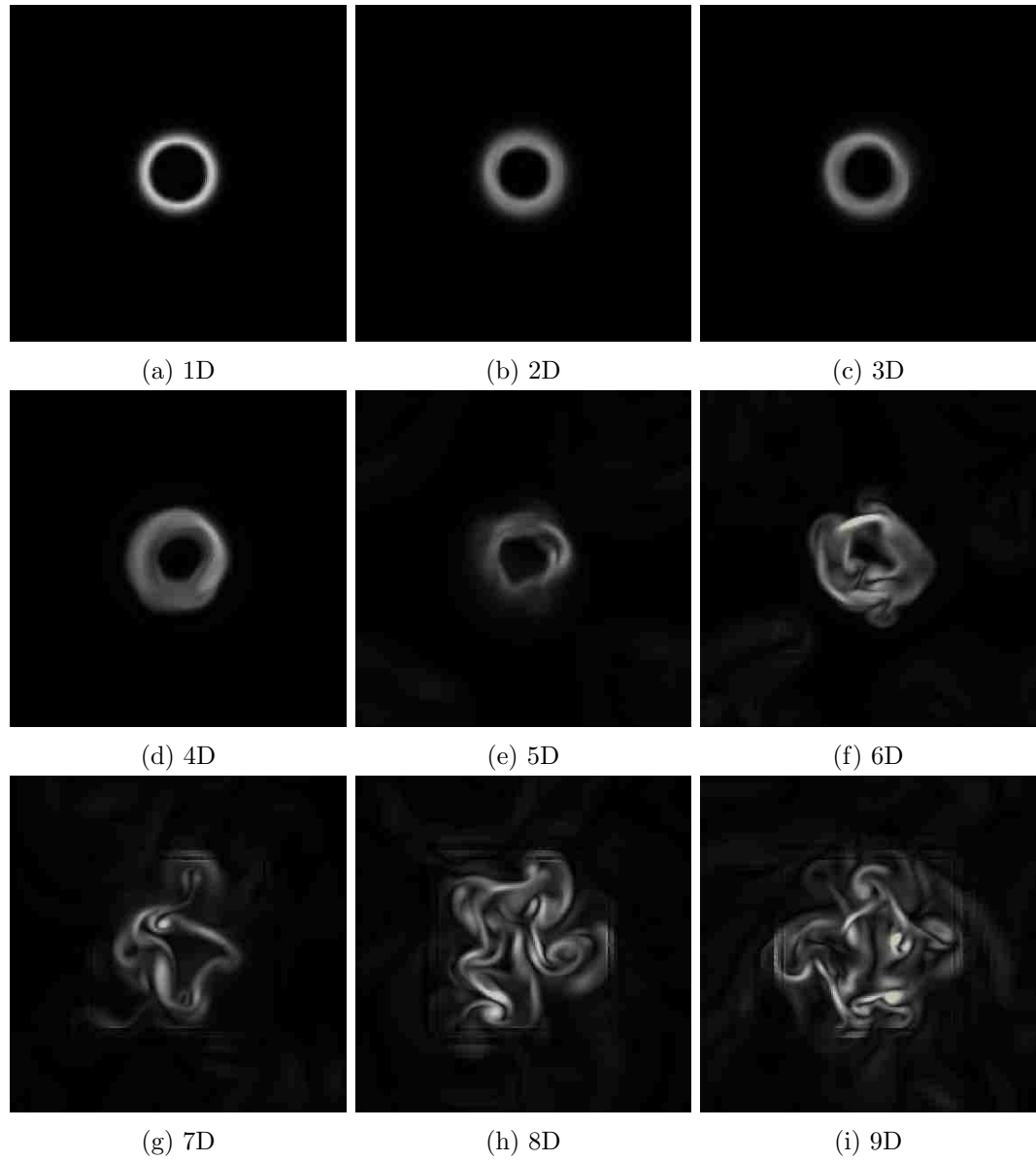
Figure 4.6: Contours of instantaneous vorticity for Re = 1620. Images are acquired at appointed cross-sections away from orifice.

4.3   Centerline Mean Velocity

Since the fluid in the tank is at rest initially, we should not consider presenting the flow field before the effect of impulsive start of flow is faded. We skip the initialization stage. The velocity and the vorticity data before 10s are not saved, and time averaging is conducted e from 10s to 30s. For better comparison, the centerline mean velocity is scaled with the inlet velocity, which is defined by

$$U^* = \frac{\overline{|\boldsymbol{U}|}}{|\boldsymbol{U}_0|}$$

Closed-up View of Centerline Mean Velocity (Scaled)
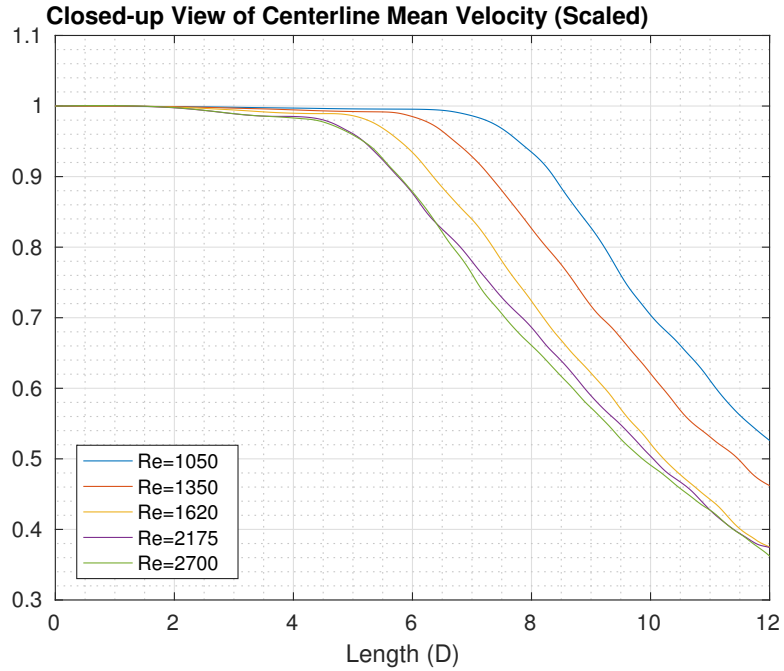
Figure 4.7: The centerline velocity as a function of normalized length for various values of Reynolds number.

In the figure shown above, the length D denotes the orifice diameter. The simulation domain has 20D in total in z-axis, but results after 10D are no longer valid, since it is impossible to trace vortices accurately for such a long distance.

For lower values of Reynolds number, that the normalized centerline velocity remain near unity U^* for a long distance away from the orifice. At Re = 1050, the centerline velocity is

nearly constant within $X/D = 6.5$ and decays linearly in the stream-wise direction beyond X of 6.5D. Crow and Champagne(1971)[7] and Burattini(2004)[4] also reported the similar behavior. They demonstrated that the centerline velocity linearly decreases after $X/D = 8$ with a slope of about -0.086.

Unlike the reference experiments, there's no significant *plateau* area where the velocity drops by 5% after exit section. In all cases U^* keep constant before $X/D = 2$. For Re=2175 and Re=2700 it is seen a 2% drop until $X/D = 4$. The centerline velocity decays with the similar slope for all flow rates considered in this study. Detailed information about the profile of the centerline velocity is shown in the Table 4.2 for various values of Reynolds number.

Re	1050	1350	1620	2175	2700
Decay from	6.50D	5.75D	4.75D	4.25D	4.25D
U^* at 10D	0.700	0.625	0.525	0.500	0.480
Decay slope	-0.086	-0.088	-0.090	-0.087	-0.090

Table 4.2: Details of the time-averaged centerline velocity listed for various values of Reynolds number.

4.3.1 Mesh Study

Although LES has a loose limitation of the mesh size comparing to DNS, it still needs to run on a finer mesh against RANS. The influence of mesh size should be considered to satisfy the minimum resolution required. We did simulation on another mesh with 1.2x higher resolution to find the difference of centerline mean velocity profile in Figure 4.8. It can be seen that there is no significant difference in the centerline velocity obtained by two different mesh sizes. Beyond $X/D = 8$ two profile show a slight deviation. That is expected the flow in this area becomes fully turbulent with small and large scale eddies. In order to capture flow structures in this area very fine mesh is needed. Since we only concern about the secondary flows evolve, the mesh with 800 nodes in z-axis is sufficient to ensure spatial convergence to predict the development of the secondary flows in early stage.
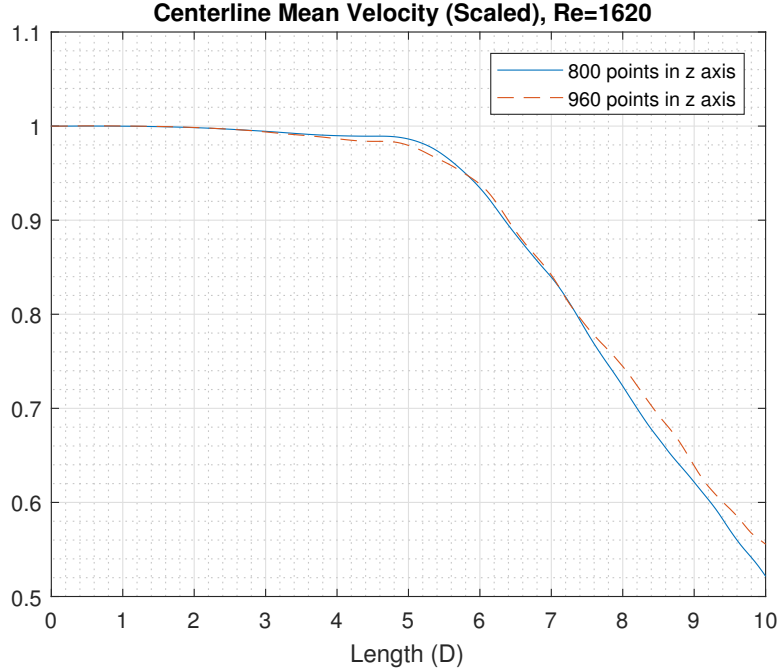
Figure 4.8: The centerline velocity vs the normalized length obtained by two different mesh density at Re=1620.

4.4 Turbulent Intensity

The turbulent intensity, referred to as T_u, is defined as the root mean square of centerline velocity fluctuation scaled with the inlet velocity. In the reference experiment, T_u increases to the first peak from the exit at around $X/D = 5$, then decreases to the dwell value at around $X/D = 7$. A second global peak value is reached at $X/D = 10$, leading to a stable plateau.

However, in our simulation the characteristic is different as shown Figure 4.9. At the orifice T_u do not start from 0. This is attributed to the introduction of disturbances at the orifice.. Turbulent intensity profiles do not display the first peak and the valley observed in the experiment. Only inflection points are shown in low values of Reynolds number. After the global peak value, T_u decreases rapidly to ground in all cases. This could happen since simulation results after $X/D = 10$ is no longer precise. If we plot our predicted results along with the results obtained by the experiment in the same figure our predicted profiles

would partially coincides with the profiles obtained by the experiment between the dwell and the second peak. The location and the magnitude of inflection and the peak are listed in Table 4.3 for various values of Reynolds number.
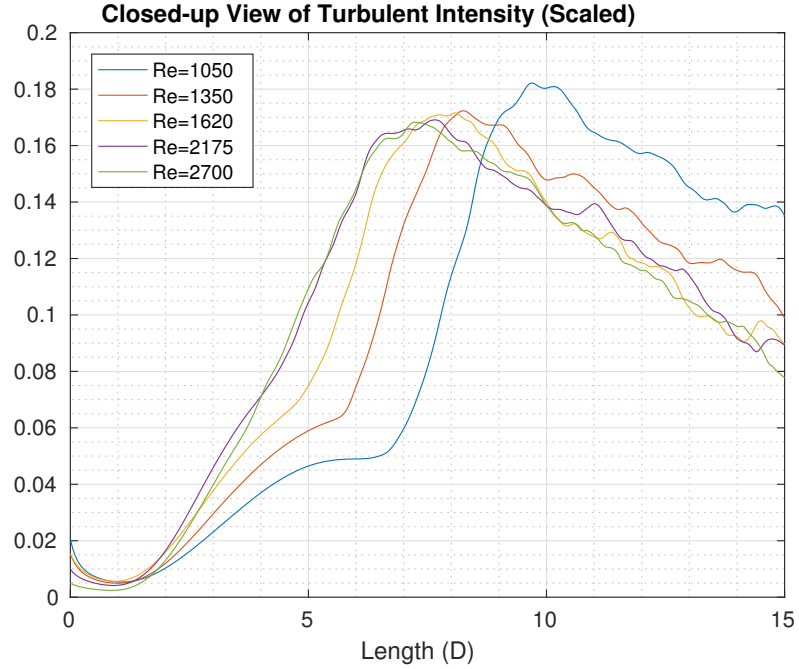
Figure 4.9: The turbulent intensity as a function of normalized length for various values of Reynolds number.

Re	Inflection location	Inflection level	Peak location	Peak level
1050	6.00D	5.00%	9.50D	18.50%
1350	5.75D	6.25%	8.25D	17.25%
1620	4.75D	6.75%	6.75D	17.00%
2175	N/A	N/A	7.50D	16.50%

Table 4.3: Details of turbulent intensity profiles for various values of Reynolds number.

Although our results of T_u didn't show corresponding double peak observed in the experiment, Meslem(2014)[16] has the similar one-peak shape and a 15% peak level. Further investigations are needed to focus on different sub grid scale models to find out the correct tendency of the turbulent intensity profiles in these flows.

4.5 Spectra Analysis

Figure 4.10 shows the velocity signal at various locations in a 2-second time window. From the figure, the aptitude of signal is increasing from $X/D = 1$, corresponding to the increasing T_u in Figure 4.9. The signal shows that the flow is very orderly and periodic in the region before x of 6D. It becomes irregular and disorderly with a decreasing average as the jet is decaying beyond x of 6D.

To observe the frequency in a more straightforward way, the Fourier transform is applied to 20-second data. The flow fluctuation is transformed from time domain to frequency domain. To compare the peak more clearly, every spectrum is scaled to the root mean square of the velocity fluctuation and shifted one decade downward comparing to previous one, as the same process in the reference experiment. Figure 4.11 depicts the Fourier analysis for Re=1620. More figures can be found in Appendix A.3 and A.4. To make the spectrum distinguishable, a low-bypass filter, which is the moving average in this case, is applied to get a smooth curve.
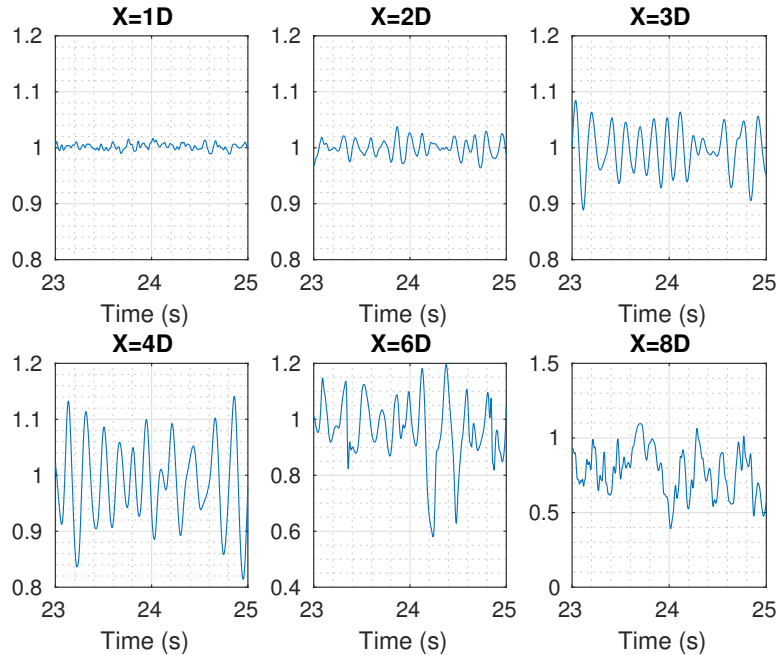
Figure 4.10: The signal of the centerline velocity at Re=1620 at various locations from the orifice. The velocity signals are plotted for two second time period.

At $X/D = 1$ there's no peak at all, where the highest peak shows at the same location in the experiment. This can be explained by the white noise we added at the inlet. It is well-known that white noises have flat frequency spectra, which means it has equal power density at all frequencies. The influence of artificial disturbance is still effective after a short distance, covering the real peak at $X/D = 1$.

As jet flow structure develops downstream, a peak is observed between 5-8 Hz at $X/D = 2$. We can discover that the peak level decreases in the vortex region. The peak frequencies are widening and moving leftward until it disappears at $X/D = 6$, where vortex breakdown occurs and energy spectra dissipates in the frequency domain. For higher values of Reynolds number, the spectrum is even flatter at $X/D = 5$, as a result of occurrence of vortex breakdown at a closer distance from the orifice. Our results in A.4 show that the higher Reynolds number is, the higher frequency the velocity signal has. Becker(1968)[1] reported an empirical frequency law that is consistent with the present study.

$$\frac{fX}{U_0} \propto \sqrt{\frac{U_0 X}{\nu}}$$

A detailed table is shown below to reveal the inherent law of fluctuation frequency. The data roughly fits the above law.

Re	2D	3D	4D	5D	6D
1050	4.0-6.0	3.5-6.0	3.0-5.5	2.5-5.0	2.0-4.5
1350	5.0-7.0	4.5-7.0	4.0-6.5	3.0-6.0	2.5-5.5
1620	6.0-9.0	5.0-8.0	4.0-7.0	3.5-6.0	N/A
2175	7.5-10.5	6.0-10.5	4.5-10.0	N/A	N/A
2700	9.0-11.0	7.0-10.5	5.0-10.0	N/A	N/A

Table 4.4: Frequency of fluctuations of the centerline velocity at various distance from the orifice for different values of Reynolds number.
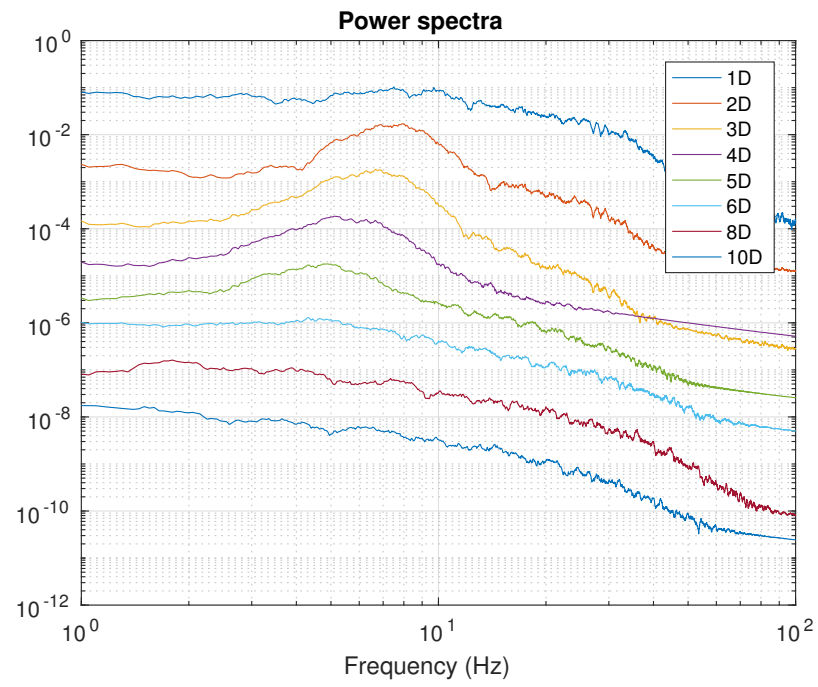
Figure 4.11: Power spectra of the velocity signals at various locations away from the orifice for Re=1620.

Chapter 5

Conclusion

A series of computational fluid dynamics simulations was performed on jet flows based on the same geometry of the experiment[20]. A cuboid domain contains fluid at rest initially while the same fluid is injected through a circular orifice. Large eddy simulations are conducted for a range of Reynolds number from 1050 to 2700.

The implementation of LES filtering and Smagorinsky sub grid scale model in Open-FOAM is presented, explained the failure on two-dimensional computational domain. Momentum predictor, the most critical component in OpenFOAM solvers, is also analyzed to show the robustness of *pimpleFOAM* with higher value of the Courant number. A non-uniform mesh with periodic boundary condition is discretized by *snappyHexMesh* utility. This universal procedure can snap the mesh to any orifice shape such as square and notched nozzles to extend the research.

Many velocity-pressure combinations of outlet boundary conditions are tested to deal with reverse flow and *pressureInletOutletVelocity* and *totalPressure* corresponds to the most realistic flow conditions. As for the inlet, a random disturbance should be added for LES to accelerate the formation of vortices. We added white noise and controlled the level with an exponential model so that more simulations can be done at different values of Reynolds number.

Visualization of velocity and vorticity fields are processed using both instantaneous

images and temporal statistics, showing the secondary flow induced by Kelvin Helmholtz instabilities. We observed the same phenomenon as the validation of flow schematics. The behavior of secondary flows is strongly dependent on Reynolds number as distinct types of vortex paring. A cross-sectional view is interpolated to provide a new perspective to demonstrate the evolution of secondary flows.

Normalized centerline mean velocity indicates that it remains near unity until it decays with the similar slope. The centerline turbulent intensity is also compared. Although the expected double peak[20] did not appear, inflection points with similar tendency can be seen on other literatures[16]. These results agree with existing experimental observations to validate the physical and mathematical model we applied.

The spectra analysis was performed by applying Fast Fourier Transform. Due to the artificial white noise at the inlet, the peak near orifice is covered by noise energy. The frequency of velocity signal increases as Reynolds number goes higher but decreases as distance from orifice is increased, which roughly fits the frequency relationship reported[1]. After vortex breakdown no peak is spotted, indicating the dissipation of vortex energy.

The above researches provides notable information about free jets. It can be applied to various scenarios such as combustion chambers and spray nozzles. Future researches will focus on the orifice shape, including square and notched nozzles, to investigate its influence on the primary and the secondary flows and turbulence mixing characteristics.

Bibliography

[1] Henry A Becker and TA Massaro. Vortex evolution in a round jet. *Journal of fluid mechanics*, 31(03):435–448, 1968.

[2] Joseph Boussinesq. *Essai sur la théorie des eaux courantes*. Imprimerie nationale, 1877.

[3] Jonas Bredberg. On the wall boundary condition for turbulence models. 2000.

[4] P Burattini, RA Antonia, S Rajagopalan, and M Stephens. Effect of initial conditions on the near-field development of a round jet. *Experiments in fluids*, 37(1):56–64, 2004.

[5] I Celik. Random flow generation technique for large eddy simulations and particle-dynamics modeling. *Journal of Fluids Engineering*, 123:359–371, 2001.

[6] Agnimitro Chakrabarti, Qin Chen, Heather D Smith, and Don Liu. Large eddy simulation of unidirectional and wave flows through vegetation. *Journal of Engineering Mechanics*, 142(8):04016048, 2016.

[7] S Cj Crow and FH Champagne. Orderly structure in jet turbulence. *Journal of Fluid Mechanics*, 48(03):547–591, 1971.

[8] James W Deardorff. A numerical study of three-dimensional turbulent channel flow at large reynolds numbers. *Journal of Fluid Mechanics*, 41(02):453–480, 1970.

[9] Massimo Germano, Ugo Piomelli, Parviz Moin, and William H Cabot. A dynamic subgrid-scale eddy viscosity model. *Physics of Fluids A: Fluid Dynamics*, 3(7):1760–1765, 1991.

[10] S.J. Kline, D.E. Coles, E.A. Hirst, United States. Air Force. Office of Scientific Research, and Stanford University. Thermosciences Division. *Computation of Turbulent Boundary Layers*. Thermosciences Division, Stanford University, 1969.

[11] Andrei N Kolmogorov. The local structure of turbulence in incompressible viscous fluid for very large reynolds numbers. In *Dokl. Akad. Nauk SSSR*, volume 30, pages 301–305. JSTOR, 1941.

[12] A Leonard. Energy cascade in large-eddy simulations of turbulent fluid flows. *Advances in geophysics*, 18:237–248, 1975.

[13] Dongyue Li. icofoam analysis. `http://dyfluid.com/icoFoam.html`.

[14] Douglas K Lilly. A proposed modification of the germano subgrid-scale closure method. *Physics of Fluids A: Fluid Dynamics*, 4(3):633–635, 1992.

[15] The OpenFOAM Foundation Ltd. `https://github.com/OpenFOAM/OpenFOAM-dev/tree/master/applications/solvers/incompressible/pimpleFoam`.

[16] Amina Meslem, Remy Greffet, Ilinca Nastase, and Amina Ammar. Experimental investigation of jets from rectangular six-lobed and round orifices at very low reynolds number. *Meccanica*, 49(10):2419–2437, 2014.

[17] KB MQ Zaman, FY Wang, and NJ Georgiadis. Noise, turbulence, and thrust of subsonic freejets from lobed nozzles. *AIAA journal*, 41(3):398–407, 2003.

[18] P ONeill, J Soria, and D Honnery. The stability of low reynolds number round jets. *Experiments in fluids*, 36(3):473–483, 2004.

[19] Joseph Smagorinsky. General circulation experiments with the primitive equations: I. the basic experiment. *Monthly weather review*, 91(3):99–164, 1963.

[20] Valentino Todde, Pier Giorgio Spazzini, and Mats Sandberg. Experimental analysis of low-reynolds number free jets. *Experiments in fluids*, 47(2):279–294, 2009.

[21] T. Von Kármán. *Mechanische Ähnlichkeit und Turbulenz*. Sonderdrucke aus den Nachrichten von der Gesellschaft der Wissenschaften zu Göttingen : Mathematisch-physische Klasse. Weidmannsche Buchh., 1930.

[22] D.C. Wilcox. *Turbulence Modeling for CFD*, volume 1. DCW Industries, 2006.

Appendix A

Additional Figures

Figure A.1 depicts profiles of the time-averaged centerline velocity in the stream-wise direction for various values of Reynolds number. In the region near the outlet the centerline velocity profiles are all similar at all values of Re; indicating that the boundary conditions imposed at the outlet are not influencing the jet flows near the orifice.

(a) Re=1050

(b) Re=1350

(c) Re=1620

(d) Re=2175
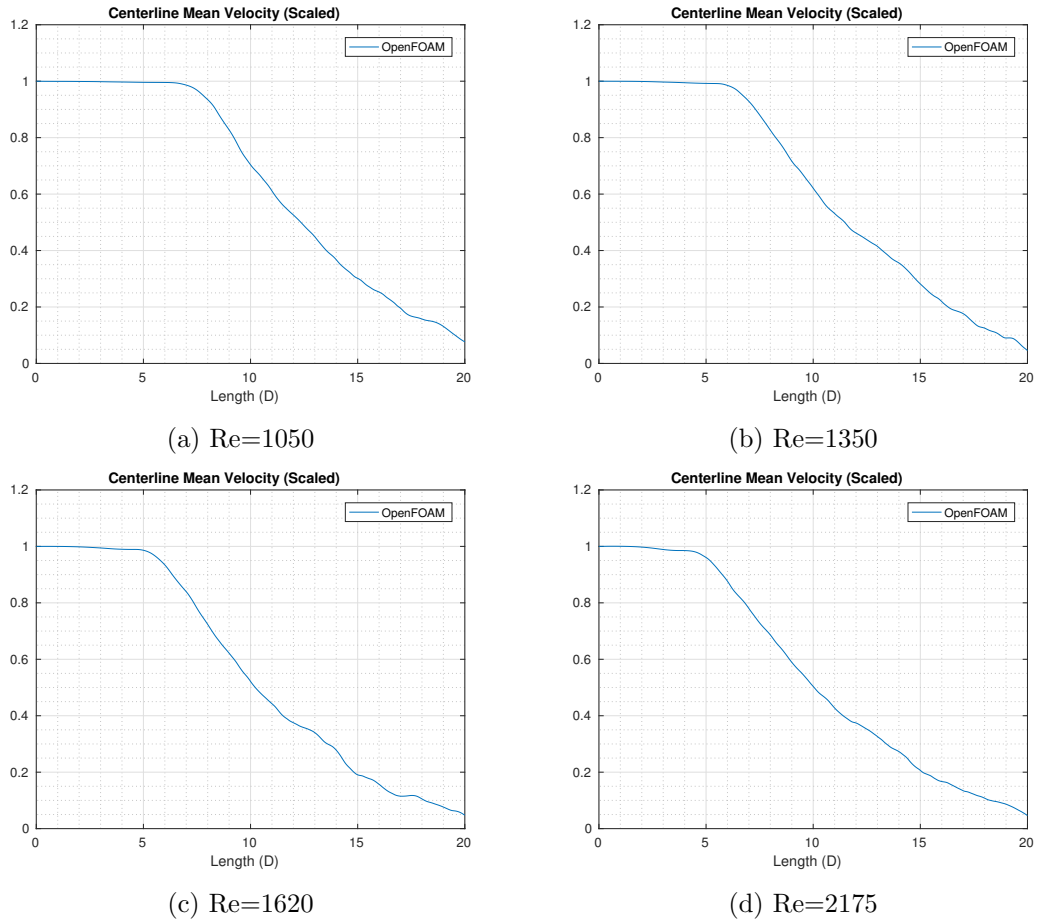
Figure A.1: The time-averaged centerline velocity is plotted as a function of the normalized length for various Re.

Figure A.2 depicts profiles of the centerline turbulent intensity in the stream-wise direction. At all values of Reynolds number, turbulent intensity profiles assume maximum and decay rapidly following the peak. Rapid dissipation of turbulence imply that the outlet boundary condition is realistic.

(a) Re=1050

(b) Re=1350

(c) Re=1620

(d) Re=2175
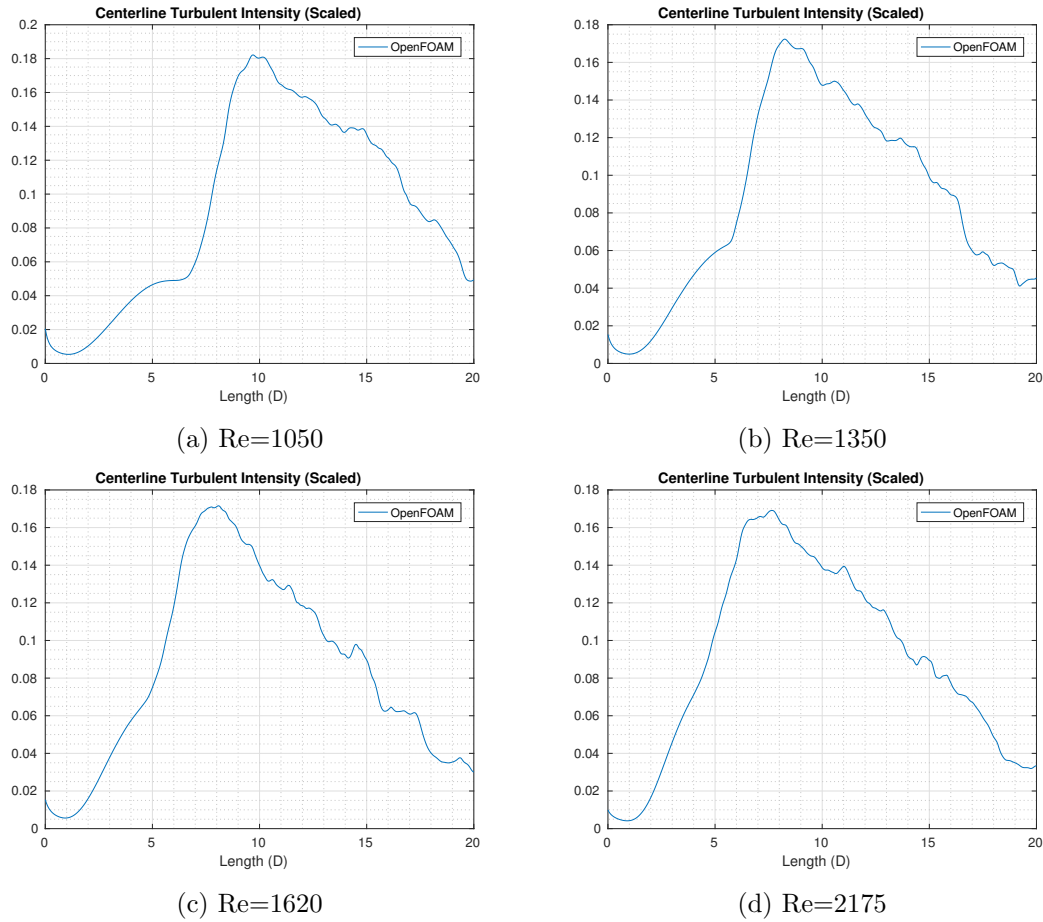
Figure A.2: The turbulent intensity is plotted as a function of the normalized length for various Re.

Figure A.3 displays signals of the centerline velocity at various distance from the orifice. The time signals are obtained for two-second time period. Amplitudes of fluctuations increases as the distance from the orifice increases. It is also indicated that the amplitude of fluctuations are greater for jet flows at higher Re.

(a) Re=1050

(b) Re=1350

(c) Re=2175

(d) Re=2700
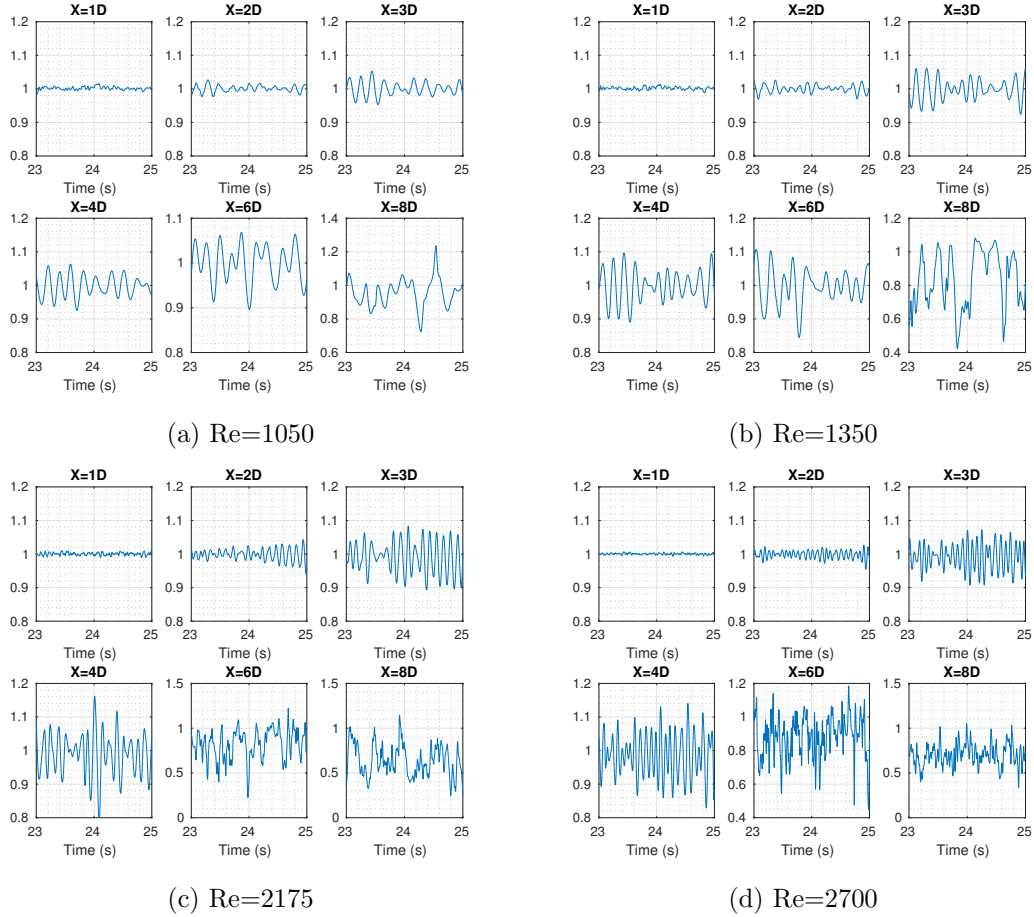
Figure A.3: The signal of the centerline velocity at various locations from the orifice for various Re. The velocity signals are plotted for two second time period.

Figure A.4 depicts power spectra of the centerline velocity signals for various values of Reynolds number. They are determined by applying fast Fourier transform to velocity signals shown in Figure A.3. Frequency of fluctuations increases as Reynolds number increases.

(a) Re=1050

(b) Re=1350

(c) Re=2175

(d) Re=2700
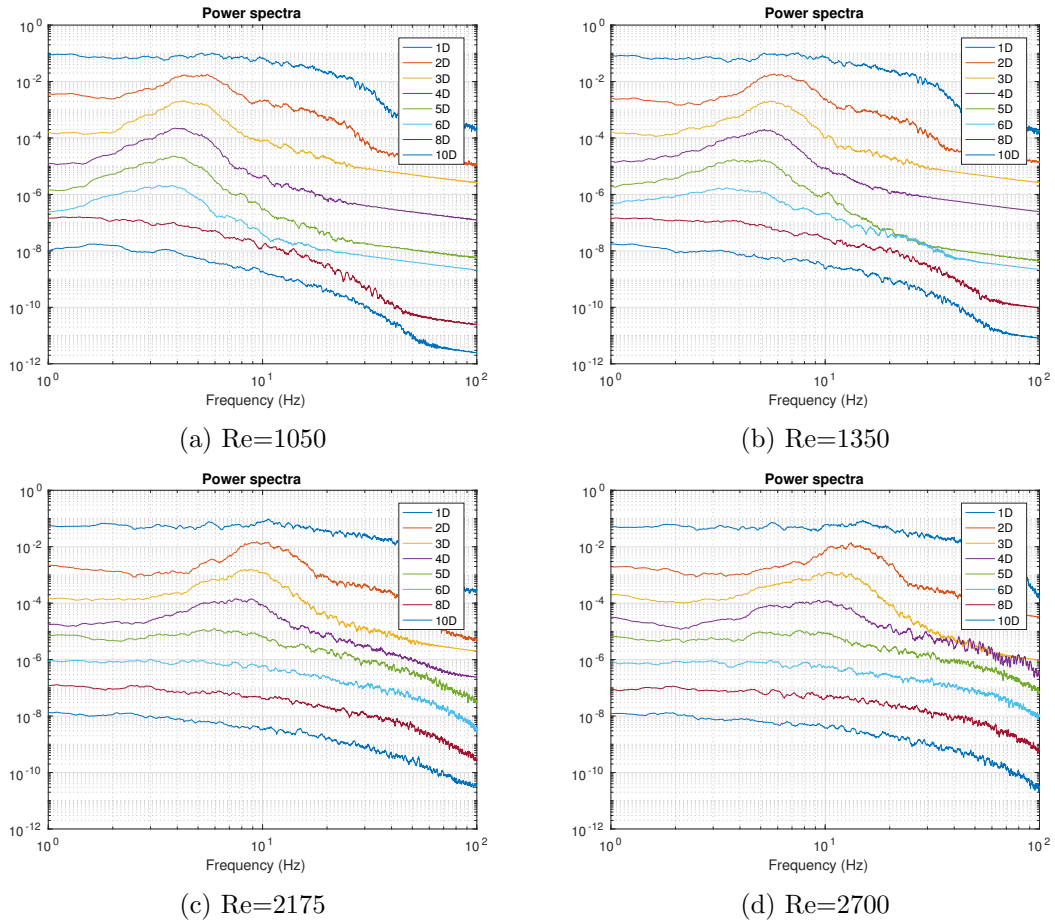
Figure A.4: Power spectra of the velocity signals at various locations away from the orifice for various Re.

Biography

Guanyang Xue was born in Beijing, China in Oct.24, 1992. He completed his bachelor of science degree in Mathematicsin Beihang University (previously known as Beijing University of Arenautics and Astronautics). Afterwards he entered the The P.C. Rossin College of Engineering and Applied Science at Lehigh University to persue his his Master of Science degree. He also participated the Industrial Assessment Center program at Lehigh University.